Appl. Phys. B 76, 569–582 (2003)
DOI: 10.1007/s00340-003-1105-y

Applied Physics B
Lasers and Optics

J.F. POWER

Linear Tikhonov regularization against an edge field: an improved reconstruction algorithm in photothermal depth profilometry

Department of Chemistry, McGill University, 801 Sherbrooke St. W., Montreal, Quebec H3A 2K6, Canada

Received: 19 September 2002
Published online: 5 May 2003 •

ABSTRACT This work introduces the concept of edge-field regularization into photothermal inverse depth profilometry problems. An edge field allows prior information concerning the depth location of material interfaces in a sample to be introduced into a Tikhonov regularization problem by a simple binary encoding. The edge-field regularization allows Nth-order Tikhonov stabilization constraints to be applied independently to multiple zones or segments of a depth profile between defined interface positions. This allows the reconstruction of continuous depth-profile information within known layers, without the globally imposed smoothing and edge oscillations of the classical regularization methods. This method successfully reconstructs both the amplitude of the interface discontinuities and the photothermal depth-contrast variations within the bounding edges, to a resolution limited by the resolving kernel for the underlying Nth-order Tikhonov constraint. The edge-field regularization dramatically reduces the errors associated with profiling photothermal contrast in bounded zones that are depth-displaced in the sample.

PACS 44.05.+e; 44.10.+i; 44.15.+a

1 Introduction

Photoacoustic and photothermal detection methods have attracted much interest over the past two decades because of their high sensitivity, and capabilities to non-destructively sense the depth variation of thermal and/or optical properties of materials on micron to submillimeter length scales. From the middle 1980's [1–8], a major effort has developed inverse problem theories that map the depth profiles of thermal and/or optical properties of solids from photothermal signals, with no prior knowledge of the sample beyond elementary assumptions of profile smoothness.

The photothermal inverse problems may be classified into three types. The type-I problem applies when the sample's thermal properties are approximately depth-constant while the optical properties vary [1, 3, 5–7]. The information of interest is the sample's depth-variable optical absorption coefficient, which may be reconstructed from the photothermal signals. This problem has attracted recent interest in tissue diagnostics [6–9] as well as in measurements on polymer films [10]. The type-II problem [2, 4, 11–13] applies when the sample is surface-heated by modulated optical absorption and there is no volume heat generation in the bulk. Thermal waves generated at the sample surface diffuse into the bulk and interact with subsurface interfaces by processes analogous to reflection or damping [14, 15]. The signature of these interactions appears in the surface photothermal data, which is used to reconstruct a depth profile of the material's thermal effusivity or, with assumptions, the diffusivity and/or conductivity. This problem has been of recent interest in metallurgical problems [16–18], addressing near-surface hardening [17] and carburization [16] in steels. The third problem, type III [19, 20], uses the measured photothermal data to map both thermal and optical properties depth contrast in a material that is subsurface-heated by optical absorption. This problem is more difficult than either type I or II, has been addressed in fewer published works and more readily delivers non-unique solutions.

Detailed examinations of these inverse problems have shown a number of common features regardless of formulation as type I, II or III, and regardless of the specific photothermal detection technique applied. These problems may all ultimately be cast in the form of first-kind Fredholm integral equations ((1), below) [21]. Their common features can be traced to the class of heat-conduction kernels (Green's functions) that underlie the Fredholm theory of photothermal detection [15]. Because the heat-conduction process is dissipative [15], the associated inverse problems are severely ill conditioned [5–7, 21, 22]. Signals based on heat diffusion act as extreme low-pass filters of depth information: the information associated with steps and edges in a material is highly attenuated in the measured signals.

This filtering effect may be directly assessed in a heat-conduction problem by a singular value analysis of the relevant Green's function underlying the detection theory [6, 21, 22]. Associated theories of regularization [21–23] apply smoothing/stability constraints to the solution that suppress the effects of data and computational errors in the recovered depth profiles. These regularization constraints ensure that the recovered depth profile is stable in the presence of data errors (e.g. small random and bias errors) at the levels encountered

✉ Fax: +1-514/398-3797, E-mail: joan.power@mcgill.ca

in the experiment. The degree of smoothing that must be applied to ensure stability of a depth profile increases as the experimental error levels in the data. Oscillations may also appear in the vicinity of reconstructed edges as the result of spectral leakage effects [21, 22], which also apply in these problems. The peak signal amplitudes of sharp depth-profile features may be seriously attenuated in the reconstructions. These effects may be partially compensated by adding constraints to the solution such as positivity or supports requiring zero amplitude outside of a defined region [24]. However, the spatial resolution limits remain a fundamental problem in both depth reconstruction and interpretation [5–7]. It may be impossible to determine if a computed profile is discrete or continuous under certain conditions [25]. The reconstruction of a truncated depth profile of (otherwise) continuous optical absorption has been a classical challenge to the type-I reconstruction problem in both biomedical [6–9, 25] and materials science applications [10–14, 16–18].

Appreciation of these resolution limits as fundamental in origin requires that information from alternate depth probes and/or from prior knowledge of the sample construction be considered. It will be shown in this work that, given a basic knowledge of the location of sample interfaces from alternate methods, the introduction of these into the photothermal inverse problem yields dramatic improvements in the profile accuracy.

While more alternative optical probes [21] have become available to address composition analysis with depth [21], photothermal methods still retain the advantages of outstanding sensitivity, as well as optical absorption and thermal depth contrast. The thermal contrast mechanism remains essentially unique, while the optical absorption contrast is shared with few other methods, exceptions being attenuated reflectance [26] (which tends to be even more ill posed and accesses much shallower depth ranges), more recently, dual-beam light-profile microscopy [27, 28] (which yields an absorption contrast with substantially poorer sensitivity) and opto-acoustic depth profilometry (restricted mainly to media with matched acoustical properties over depth) [29]. Recent methods that depth profile by contrast complementary to photothermal methods include low-coherence optical reflectometry [30, 31], confocal microscopy [32] and (single-beam) light-profile microscopy [27].

In this work, a new form of regularization is introduced into the photothermal reconstruction problem that incorporates interfacial information from such probes, or from prior knowledge of the sample reconstruction. This form was first formulated by Terzopolous [33] for the relatively well-conditioned inverse problems of early vision reconstruction. While it has been used extensively in this class of problems (see [34, 35] and references therein), it has not previously been applied to the severely ill-posed photothermal inverse problems. By introducing the construct of an edge field into the classical regularization operator [33], a modified form of the familiar Tikhonov regularization is obtained, having the special properties of edge-constrained profile smoothing. While the original Tikhonov regularization applies global smoothing over the entire depth space in a reconstruction problem, the edge-field regularization allows profile stabilization to be applied independently in an arbitrary number of bounded zones in the depth space [33]. This implementation, as put forth below, requires an approximate knowledge of the interface locations, but not the amplitudes of the interfacial contrast changes, as these are determined by the reconstruction. Unlike conventional Tikhonov regularization, which distributes errors in profile reconstruction globally over the model space, in edge-field regularization, errors in profile fitting are segmented and independent of errors in other zones [33]. It will be shown that depth-profile information inside these bounded depth zones is available with spatial resolution limited by the resolving kernel of the classical Tikhonov stabilizer. The result is that, with prior information of this type, the global errors in reconstruction, within bounded depth zones, are dramatically improved over the prior inverse methods.

2 Theoretical section

2.1 *The photothermal inverse problem*

The photothermal problems of interest may be cast in the form of a first-kind Fredholm integral [21]:

$$h(t) = \int_X G\,(x, x_0, t)\;\varrho\,(x_0)\,\mathrm{d}x_0, \tag{1}$$

where x appears as a constant parameter, $h(t)$ is the photothermal response, $G(x, x_0, t)$ is a detection kernel derived from the Green's function for one-dimensional heat conduction (with suitable modification for experimental conditions) and $\varrho(x_0)$ is a depth profile related to the thermal or optical properties of the sample; x and x_0 are standard observation and source coordinates [15, 21]. The experimental 't' coordinate may be either time or modulation frequency (the time-domain (impulse) response is emphasized below).

Depending on the specific photothermal inverse problem addressed, $G(x, x_0, t)$ is interpreted slightly differently. The type-I photothermal inverse problem [1, 3, 5–7] gives the most concrete illustration of the algorithm. Here, $\varrho(x)$ is proportional to the depth distribution of initial temperature established by light absorption of a short optical pulse [6–8]. For weak absorption $\varrho(x)$ is proportional to $\beta(x)$ [1, 3, 5], the depth-dependent optical absorption coefficient of the sample. If the sample is effectively thermally homogeneous with depth and continuous with a backing layer, the Green's function is written as $G(x - x_0, t)$ and (1) is expressed in discrete form as:

$$h\,(t_m) = \sum_{n=1}^{N} G\,(x - x_{0n}, t_m)\varrho\,(x_{0n})\;\Delta x_n \tag{2}$$

or, equivalently, in matrix form as:

$$\mathbf{h} = \mathbf{G} \times \mathbf{p}\,, \tag{3}$$

where $\mathbf{h}(M \times 1)$ and $\mathbf{p}(N \times 1)$ are column vectors containing discrete approximations to $h(t)$ and $\varrho(x)$; $\mathbf{G}(M \times N)$ (with $M \geq N$ in general) approximates the kernel in (1).

Because of ill conditioning, as is well known in photothermal inverse problems [5–7, 16], regularized least-squares

methods must be introduced to evaluate a stable approximation to the inverse of (3). A common strategy is to use orthogonal decompositions such as the singular value decomposition (SVD) [23]:

$$\mathbf{G} = \mathbf{U} \times \mathbf{m} \times \mathbf{V}^{\mathrm{T}}, \tag{4a}$$

where $\mathbf{U}(M \times M)$ and $\mathbf{V}(N \times N)$ are matrices containing orthogonal sets of left and right singular vectors of $\mathbf{G}$, and $\mathbf{m}$ is an $(M \times N)$ matrix having as entries μ_i, the singular values of $\mathbf{G}$, ordered along its diagonal, and zeros elsewhere. Subject to editing to zero (truncation) of the contribution of sufficiently small μ_i [6, 21–23] in the inverse matrix $\mathbf{m}^{-1}$, the pseudo-inverse of $\mathbf{G}$ is then computed as:

$$\mathbf{G}^{+} = \mathbf{V} \times \mathbf{m}^{-1} \times \mathbf{U}^{\mathrm{T}}. \tag{4b}$$

This gives rise to a least-squares estimate $\mathbf{p}^{+}$ subject to the condition of minimum modulus (see [23] and references therein):

$$\mathbf{p}^{+} = \mathbf{G}^{+} \times \mathbf{h}. \tag{4c}$$

A closely related strategy has been to use the zero-order Tikhonov regularization, in which a least-squares solution profile is computed, having the (schematic) form [23]:

$$\mathbf{p}^{+} = \left[\mathbf{G}^{\mathrm{T}}\mathbf{G} + \boldsymbol{\lambda}^2\mathbf{I}\right]^{-1}\mathbf{G}^{\mathrm{T}}\mathbf{h}, \tag{5}$$

where the constant $\boldsymbol{\lambda}$ is a regularization parameter, revisited below.

It has been shown [23] that the regularization operation in (5) acts tantamount to the editing (truncation) of small singular values in the computation of (4b). Together, the strategies of SVD and zero-order Tikhonov regularization (abbreviated TR-0) account for the commonly used strategies to solve inverse problems in photothermal reconstruction. Their well-known spatial resolution limits have been discussed in a number of previous works [5–7, 12, 21, 22, 25].

The present algorithm using an edge-field constraint makes use of the nth-order Tikhonov regularization (abbreviated TR-n) (of which (5) gives a special case for $n = 0$ and $\mathbf{L}_n = \mathbf{I}$). This problem is posed as the minimization of an error norm [23]:

$$S_p^2 = \|\mathbf{h} - \mathbf{G} \times \mathbf{p}\|_2^2 + \boldsymbol{\lambda}^2 \|\mathbf{L}_n \times (\mathbf{p} - \mathbf{p}_0)\|_2^2, \tag{6}$$

where the least-squares error S_p^2 is expressed as the sum of two error norms: a chi residual that forces agreement between the data and the fitted model:

$$\chi^2 = \|\mathbf{h} - \mathbf{G} \times \mathbf{p}\|_2^2, \tag{7}$$

and a side constraint or stabilizer term defined as:

$$S_{\mathrm{s}}^2 = \|\mathbf{L}_n \times \mathbf{p}\|_2^2. \tag{8}$$

The profile $\mathbf{p}_0$ that appears in (6) contains prior information about the depth structure but is assumed to be zero in the present discussion. The stabilizer term imposes a condition of smoothness into the recovered profile. In the case TR-n discussed here, $\mathbf{L}_n$ is a difference operator giving a discrete approximation to the nth-order spatial (x) derivative of the profile $\mathbf{p}$ [23, 36]. Minimizing the stabilizer term is therefore equivalent to minimizing the nth-order derivative of $\mathbf{p}$. This, in turn, amounts to allowing $\mathbf{p}$ to be approximated by an $(n-1)$th-order polynomial of arbitrary form: $p_{n-1}(x) = a_0 + a_1 x + a_2 x^2 + \ldots a_{n-1}x^{n-1}$. Hence (6) poses the least-squares problem as a minimization of differences between the data and fitted model, subject to the constraint that $\mathbf{p}$ is smooth in the sense of an $(n-1)$th-order polynomial (whose coefficients are determined in the course of the fit [36]).

The least-squares solution to (6) is obtained (schematically) from a set of normal equations per the expression [23]:

$$\mathbf{p}^{+} = \left[\mathbf{G}^{\mathrm{T}}\mathbf{G} + \boldsymbol{\lambda}^2\mathbf{L}_n^{\mathrm{T}}\mathbf{L}_n\right]^{-1}\left(\mathbf{G}^{\mathrm{T}}\mathbf{h} + \boldsymbol{\lambda}^2\mathbf{L}_n^{\mathrm{T}}\mathbf{L}_n\mathbf{p}_0\right), \tag{9}$$

a framework that the present algorithm makes use of for the case $\mathbf{p}_0 = 0$.

The zero-order Tikhonov regularization [23] (TR-0) specially makes use of the side constraint $\mathbf{p} = 0$, which acts as a smoothing operator on the solution. The $n = 1$ order extends this constraint to $\mathbf{p} = \text{const.}$ (not necessarily zero). Hence, the $\mathbf{L}_1$ difference operator must minimize a discrete approximation to the first derivative of $\mathbf{p}$. This is expressed by the following band-diagonal $((N-1) \times N)$ matrix [36]:

$$\mathbf{L}_1 = \begin{bmatrix} -1 & 1 & 0 & 0\ldots & 0 \\ 0 & -1 & 1 & 0\ldots & 0 \\ 0 & & & & \\ . & & & & \\ . & & & & \\ 0 & 0 & \ldots & -1 & 1 \end{bmatrix}, \tag{10}$$

from which we obtain the following expression for the side constraint S_{s}^2:

$$S_{\mathrm{s}}^2 = \|\mathbf{L}_1 \times \mathbf{p}\|_2^2 = \mathbf{p}^{\mathrm{T}}\mathbf{L}_1^{\mathrm{T}}\mathbf{L}_1\mathbf{p} = \sum_{i=1}^{N-1}(p_{i+1} - p_i)^2, \tag{11}$$

which clearly expresses the side term S_{s}^2 as proportional to the sum of squares of the discrete first derivative of $\mathbf{p}$.

2.2 *Incorporation of discontinuities into the solution profile*

We now introduce discontinuity information into the solution. An advantage of $n = 0$ Tikhonov regularization is the well-defined filtering or smoothing operation that is imposed on the solution profile. While TR-0 is well known to provide stable reconstructions of slowly varying profiles, a key limitation is that the side constraint directs $\mathbf{p}$ to minimize to a single (zero-valued) constant over the entire depth space [33]. This stabilizes the inverse of (3) at the expense of smoothing the entire solution profile, including any edges or discontinuities that may be present. The TR-1 solution, which also directs minimization to $\mathbf{p}^{+} = \text{const.}\ (\neq 0)$, does not provide significant improvement. Figure 1 shows an example of the typical reconstruction of a flat-top or 'box' profile. In addition to smoothing of the profile edges, oscillations may also occur. These are at-

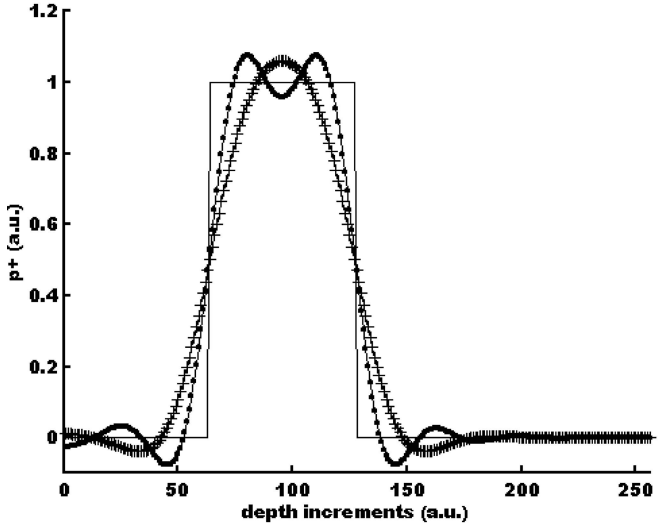

FIGURE 1 Reconstruction of an edge by various Tikhonov regularization orders at a regularization level $\lambda_0 = 0.01$: ————, theory; -+-+-+, $n = 0$ order reconstruction; -.-.-.-, $n = 1$ order reconstruction

tributable to a spectral leakage effect (Gibbs phenomenon) introduced by the regularization (see [21, 23] and references therein).

The key to improved TR-type depth-profile reconstructions over zones bounded by edges is the introduction of a so-called line-field operator [33, 34] into the regularization functional, $\mathbf{L}_n$. The line field [34] is a development from the field of early vision [33] reconstruction that allows systematic introduction of bounding edges into a profile that is piecewise-continuous. The concept was given extensive development in the work of Terzopolous [33], and was used more recently in parallel algorithms implemented for early vision reconstruction [34].

The line-field concept works on the principle of allowing discontinuities to appear in the derivatives minimized in (11) [33]. The line field works by setting to zero terms in the square error summation of (11) at the location of physical interfaces. For example, if an interface occurs at depth x_j, a zero weight is set for the term $(p_j - p_i)$, thereby allowing the condition $(p_k - p_j) \neq (p_j - p_i)$ to occur. Setting the jth term to zero in (11) amounts to forcing the jth row of the $\mathbf{L}_1$ difference operator to zero. This modification can be summarized by a line field operator, $\mathbf{v}$, defined as [34]:

$$\mathbf{v} = \mathrm{diag}\left[(1 - v_i)^{1/2}\right], \tag{12}$$

where $\mathbf{v}$ is $(N-1) \times N$ and $v_i = 1$ if an interface is present and $v_i = 0$ otherwise. From this we may define the modified regularization operator [34]:

$$\mathbf{M}_1 = \mathbf{v} \times \mathbf{L}_1, \tag{13}$$

so that (11) is modified to:

$$\mathbf{M}_1^{\mathrm{T}} \times \mathbf{M}_1 = (\mathbf{v} \times \mathbf{L}_1)^{\mathrm{T}} (\mathbf{v} \times \mathbf{L}_1) = \sum_{i=1}^{N-1} (p_{i+1} - p_1)^2 (1 - v_i)\,. \tag{14}$$

Introducing this side constraint into (9) and assuming that $\mathbf{p}_0 = 0$, we now write the following (schematic) solution to the normal equations for the solution profile [34]:

$$\mathbf{p}^+ = \left[\mathbf{G}^{\mathrm{T}}\mathbf{G} + \boldsymbol{\lambda}^2 \mathbf{M}_1^{\mathrm{T}} \mathbf{M}_1\right]^{-1} \mathbf{G}^{\mathrm{T}}\mathbf{h}. \tag{15}$$

Equations (13)–(15) assume an $\mathbf{L}_1$ difference operator to appear in the side constraint, but the line-field construct may be extended to general (n) order. In the present work, $n = 1$ order is assumed for reasons discussed below.

2.3 *The inversion algorithm*

The solution to the inverse problem may now be seen as a form closely related to the Tikhonov (TR-n) form, but with continuity in the side constraint broken at specified interfaces. Subject to the assumption of available prior information, the solution of the inverse problem is obtained by entering unit 'marker' values into the $\mathbf{v}$ vector at known interface locations and then undertaking use of the normal equations as presented in (15). The direct use of this form for computation, however, has been classically proscribed [36], because of errors resulting from computation of $\mathbf{G}^{\mathrm{T}} \times \mathbf{G}$. A preferred method of solution [23, 37, 38] is via the generalized singular value decomposition (GSVD) [23, 37, 38] that for the pair of operators $\mathbf{G}$ and $\mathbf{L}$ performs a decomposition of the following form:

$$\mathbf{G} = \mathbf{U} \times \mathbf{a} \times \mathbf{X}^{\mathrm{T}}, \tag{16a}$$

$$\mathbf{L} = \mathbf{V} \times \mathbf{b} \times \mathbf{X}^{\mathrm{T}}. \tag{16b}$$

Given $\mathbf{G}(M \times N)$ and $\mathbf{L}(Q \times N)$, $\mathbf{U}(M \times M)$ and $\mathbf{V}(Q \times Q)$ (with $Q < N$) are orthogonal sets, and the matrix $\mathbf{X}(N \times N)$ is invertible, but in general not orthogonal. For the purposes of the present problem, it may be considered well conditioned. The notation posed in (16a) and (16b) is consistent with the algorithm utilized by the Matlab GSVD procedure [38]. In addition to notational differences from the literature [23, 37, 38], the Matlab procedure [38] does not explicitly require non-overlapping null spaces [23, 37] for $\mathbf{G}$ and $\mathbf{L}$, although such an overlap would produce non-unique diagonal entries in the matrices $\mathbf{a}$ and $\mathbf{b}$. The matrices $\mathbf{a}$ and $\mathbf{b}$ contain the singular values of $\mathbf{G}$ and $\mathbf{L}$, respectively, along the main diagonals, respectively, and have the block forms:

$$\mathbf{a} = \begin{bmatrix} \mathrm{diag}_Q\,(a_i) & 0 \\ 0 & \mathbf{I}_{N-Q} \end{bmatrix}, \tag{17a}$$

where the singular values are ordered in magnitude [38] as $a_1 < a_2 < a_3 \ldots < a_q < 1$, and also:

$$\mathbf{b} = \begin{bmatrix} \mathrm{diag}_Q\,(b_i) & 0 \end{bmatrix}, \tag{17b}$$

where the diagonal entries of $\mathbf{b}$ are likewise ordered $1 \geq b_1 > b_2 > b_3 \ldots > b_q$ by the Matlab GSVD algorithm.

The diagonal elements of $\mathbf{a}$ and $\mathbf{b}$ also obey the constraints [23, 37]:

$$a_i^2 + b_i^2 = 1, \tag{18}$$

and the following generalized singular values, γ_i, are further defined by:

$$\gamma_i = a_i/b_i. \tag{19}$$

The stable forms in (16a) and (16b) give rise directly to the following expressions:

$$\mathbf{G}^{\mathrm{T}}\mathbf{G} = \mathbf{X} \times \mathbf{a}^{\mathrm{T}} \times \mathbf{a} \times \mathbf{X}^{\mathrm{T}}, \tag{20a}$$

$$\mathbf{L}^{\mathrm{T}}\mathbf{L} = \mathbf{X} \times \mathbf{b}^{\mathrm{T}} \times \mathbf{b} \times \mathbf{X}^{\mathrm{T}}. \tag{20b}$$

Accordingly, we can simplify the inverted factor in parentheses in (15):

$$\left[\mathbf{G}^{\mathrm{T}}\mathbf{G} + \lambda^2\mathbf{L}^{\mathrm{T}}\mathbf{L}\right]^{-1} = \left(\mathbf{X}^{\mathrm{T}}\right)^{-1}\left[\mathbf{a}^{\mathrm{T}}\mathbf{a} + \lambda^2\mathbf{b}^{\mathrm{T}}\mathbf{b}\right]^{-1}\mathbf{X}^{-1}. \tag{21}$$

And, further, we have:

$$\mathbf{G}^{\mathrm{T}} \times \mathbf{h} = \mathbf{X} \times \mathbf{a}^{\mathrm{T}} \times \mathbf{U}^{\mathrm{T}} \times \mathbf{h}. \tag{22}$$

The solution of the least-squares problem is then written:

$$\mathbf{p}^{+} = \left(\mathbf{X}^{\mathrm{T}}\right)^{-1}\left[\mathbf{a}^{\mathrm{T}}\mathbf{a} + \lambda^2\mathbf{b}^{\mathrm{T}}\mathbf{b}\right]^{-1} \times \mathbf{a}^{\mathrm{T}} \times \mathbf{U}^{\mathrm{T}} \times \mathbf{h}, \tag{23}$$

which is entirely expressed in terms of orthogonal and/or invertible matrices.

This expression may be further simplified to obtain more insight into the filtering [23] operations used by the GSVD. From (17)–(19), we write:

$$\left[\mathbf{a}^{\mathrm{T}}\mathbf{a} + \lambda^2\mathbf{b}^{\mathrm{T}}\mathbf{b}\right]^{-1} = \begin{bmatrix} \mathrm{diag}_Q\left(\left(a_i^2 + \lambda^2 b_i^2\right)^{-1}\right) & 0 \\ 0 & \mathbf{I}_{N-Q} \end{bmatrix} \tag{24}$$

and, further,

$$\left[\mathbf{a}^{\mathrm{T}}\mathbf{a} + \lambda^2\mathbf{b}^{\mathrm{T}}\mathbf{b}\right]^{-1} = \begin{bmatrix} \mathrm{diag}_Q\left(\frac{1}{a_i^2}\frac{\gamma_i^2}{\gamma_i^2+\lambda^2}\right) & 0 \\ 0 & \mathbf{I}_{N-Q} \end{bmatrix}. \tag{25}$$

From (23) and (25) we can define a matrix of filter weights:

$$\mathbf{F} = \begin{bmatrix} \mathrm{diag}_Q\left(\frac{\gamma_i^2}{\gamma_i^2+\lambda^2}\right) & 0 \\ 0 & \mathbf{I}_{N-Q} \end{bmatrix}. \tag{26}$$

The significance of $\mathbf{F}$ as a set of filter factors weighting the singular values in the solution expansion has been discussed in detail elsewhere [21, 23]. The least-squares solution, (15), is finally expressed as:

$$\mathbf{p}^{+} = \left(\mathbf{X}^{\mathrm{T}}\right)^{-1} \times \mathbf{F} \times \left(\mathbf{a}^{\mathrm{T}}\right)^{-1} \times \mathbf{U}^{\mathrm{T}} \times \mathbf{h}\,. \tag{27}$$

This form applies equally when $\mathbf{L} = \mathbf{L}_n$ (9) or when $\mathbf{L} = \mathbf{M}_1$ (15). In the former case, we have nth-order Tikhonov regularization (TR-n) and, in the latter, first-order Tikhonov regularization in the presence of a line field. Because the present problem is one dimensional (as opposed to the three-dimensional problems of early vision), the term 'edge field' is introduced in preference to 'line field'. The edge-field entries have no special connection properties [34] and are independent. Finally, we introduce the notation LREF-1 (linear regularization with edge field, $n = 1$ order) to denote the inverse problem represented by (15).

A final case that must be considered for reference occurs in (9) for a non-zero prior $\mathbf{p}_0 \neq 0$. Application of (16)–(26) yields the following expanded form of the solution:

$$\mathbf{p}^{+} = \left(\mathbf{X}^{\mathrm{T}}\right)^{-1} \times \left[\mathbf{F} \times \left(\mathbf{a}^{\mathrm{T}}\right)^{-1}\mathbf{U}^{\mathrm{T}}\mathbf{h} + (\mathbf{I}_{N\times N} - \mathbf{F}) \times \mathbf{X}^{\mathrm{T}}\mathbf{p}_0\right]. \tag{28}$$

This form is only used here for reference (TR-1) computations that may accommodate (where specified) a constant prior.

2.4 *Testing of the algorithm*

Below, we review the results of a numerical evaluation of this algorithm made on theoretical data. The intention is to demonstrate the significant improvements in profile reconstruction that are available from this algorithm. Also, stability of the algorithm is demonstrated, and an assessment of errors is made.

The LREF-1 algorithm computes the solution profile via (27). This is based on the GSVD ((16a) and (16b)). The $\mathbf{L}$ operator is defined as $\mathbf{L} \equiv \mathbf{M}_1$ incorporating the $\mathbf{L}_1$ difference operator of (10) and the edge field $\mathbf{v}$ (12). Edge positions in the model space were introduced as unit marker values into the vector $\mathbf{v}$.

The algorithm was tested by inverting the theoretical impulse response computed for known profiles containing steps and edges. Computations of the data vector $\mathbf{h}$ were made according to the forward theory (3) for theoretical depth profiles containing well-defined edges and steps in the model space. A kernel $\mathbf{G}$ was derived based on Green's functions for heat conduction as described below. The theoretical data were inverted against a reconstruction kernel or basis, $\mathbf{G}_r$, using the same equations as $\mathbf{G}$, but for depth and time sampling that was not always identical to the forward theory. This is presented on a case-by-case basis below.

The test profiles examined in this study consisted of the following set of 'edgy' depth objects:

1. 'Flat-top' or box profile:

$$p_1(x) = U(x - x_1) - U(x - x_2) \qquad (x_2 > x_1), \tag{29a}$$

where $U(x)$ is the unit step function and x_1 and x_2 define the profile edges.

2. Truncated exponential profile:

$$p_2(x) = \exp(-\beta(x - x_1))\,[U(x - x_1) - U(x - x_2)] \quad (x_2 > x_1) \tag{29b}$$

where β is an analogous absorption coefficient.

3. Weighted bi-exponential profile:

$$p_3(x) = w_1 \exp(-\beta_1(x - x_1))\,[U(x - x_1) - U(x - x_2)] + w_2 \exp(-\beta_2(x - x_3))\,[U(x - x_3) - U(x - x_4)], \tag{29c}$$

where w_1 and w_2 are arbitrary weight factors and, in general, $x_j \geq \sum_{i=1}^{j-1} x_i$.

Finally, the kernel, $\mathbf{G}$, considered for this study was based on one-dimensional heat conduction in a semi-infinite

medium [23, 39], with the sample space assumed to occupy the depth space $0 \leq x_0 < L_{\max}$ and detection to occur at the sample surface $x = 0$. The sample is assumed to be bounded by a thermally continuous semi-infinite half-space ($x_0 < 0$) where no heat generation occurs. This geometry is pertinent (with straightforward modifications) to a number of photothermal measurement situations, including gas-microphone photoacoustic spectrometry, mirage-effect detection and infrared photothermal radiometry (at wavelengths where the emission signal is strongly absorbed). The pertinent Green's function in the continuous problem (1) is written [15, 21, 39]:

$$G\,(x - x_0, t) = \frac{A_0}{\mu_t} \exp\left(-\,(x - x_0)^2\,/\mu_t^2\right) U(t)U(x_0) \qquad (30)$$

for impulse (time-domain) excitation of the sample applied at $t = 0^+$, $x = 0$ (implicit) and $\mu_t = \sqrt{4\alpha t}$ being a thermal diffusion length, with α the thermal diffusivity. The time-domain form is preferred for ease of visualization of the heat-conduction physics.

The **G** kernel was approximated for discrete depth (x_0) and time (t) samples according to a non-uniform sampling scheme similar to that derived by Sathyam and Prahl [7]. Because of the dissipative nature of the heat conduction underlying the kernel, **G**, broadening of the depth profiles recovered by the Tikhonov regularization is systematic [5–7, 25] with feature depth. However, if time and depth coordinates are sampled uniformly over a logarithmic scale, such depth broadening is uniform on this scale [7].

In such a depth space, the coordinate x_0 is discretized so that each depth point x_{0i} is probed at some constant multiple of a base spacing, δx, from its neighbors. For example, the first depth point is located at minimum depth δx, per $x_1 = \delta x$; the second at $x_2 = a \times x_1$, the third at $x_3 = a \times x_2$ and the nth point thus at:

$$x_n = a^{n-1}\delta x, \qquad (31)$$

where 'a' is a constant radix determined below. Given that at each depth probed, the Green's function peaks in time at $t_n = {x_n}^2/2\alpha$, then the corresponding discrete-time sampling occurs at:

$$t_n = a^{2(n-1)}\delta t, \qquad (32)$$

where $\delta t = {\delta x_0}^2/2\alpha$.

The depth space in (31) is clearly uniform on the logarithmic scale:

$$\ln\,(x_n) = n \ln a + (\ln \delta x - \ln a), \qquad (33)$$

which is written to emphasize that a depth profile displayed as a function of the model increment, n, is uniformly distributed on such a scale.

The value of 'a' must be chosen to ensure uniform coverage of the basis vectors on the logarithmic scale. Given that N is the number of depth points in the reconstruction, $x_N = L_{\max}$ and the peak time for the largest depth is $t_N = {x_N}^2/2\alpha = a^{2(n-1)} \times \delta x^2/2\alpha$.

Rearrangement yields:

$$a = \exp\left(\frac{1}{N-1} \ln\,(L_{\max}/\delta x)\right). \qquad (34)$$

With this sampling, the basis, **G**, has uniform amplitude (because of the weighting by the interval $\Delta x_n = (x_{n+1} - x_n)$), and a depth-invariant time-profile envelope on the logarithmic scale. As shown below, this basis set exhibits depth broadening of the Tikhonov reconstructions that is uniform over the depth index.

The basis set is computed subject to the following conditions:
$\delta t = 5 \times 10^{-8}$ s (e.g. a 20-MHz bandwidth);
$\delta x = 1 \times 10^{-7}$ m (minimum detectable depth at a 20-MHz bandwidth);
$\alpha = 1 \times 10^{-7}\,\mathrm{m}^2/\mathrm{s}$ (close to the diffusivity of rubbery (amorphous) polymer);
$N = 256$ depth points (except where indicated);
$L_{\max} = 5 \times 10^{-4}$ m;
N time points were determined for the depth points according to the expression:
$t_n = \sqrt{2\alpha t}$.

Initially, the number of depth points used to compute **G** for the forward theory, N_s, was varied in relation to N_r, the number of depth points used in the kernel for the reverse computation. The results were convergent for the case $N_s = 1024$, $N_r = 256$, showing only small differences ($\sim 1\%$) from the case $N_s = N_r = 1024$ at the profile edges (where the depth-scale coordinates at the lower resolution did not coincide with the original synthesis points). For the reconstructions below, $N_s = N_r = 256$.

3 Results

3.1 *Broadening of the solution profile*

First, a uniform depth broadening of the solution profile $\mathbf{p}^+$ was confirmed by plotting the resolving kernel, $\delta(x, x_0)$, for the algorithm [40]. This function displays the broadening of a plane source displaced as a systematic function of depth in the model space. A plane source, $\delta(x - x_n)$, is placed at each depth in the model space, and its depth profile is reconstructed by the algorithm. This was done for first the TR-1 algorithm, which accounts for broadening both in the continuous depth space and inside (but away from) the boundary edges in the models returned by LREF-1. A basis set with parameters set as in Sect. 2 was used with a regularization parameter $\lambda_0 = 0.005$. Figure 2 shows the result for $\delta(x, x_0)$ plotted against a depth coordinate consisting of the model index n (cf. Equation (33)), which is uniform on the logarithmic scale. Except near the front and back boundaries where constraints on the depth space intervene, the broadening in $\delta(x - x_n)$ is invariant with position over the model index, with a profile half-width of $\Delta_\delta = 27$ increments (center to second zero). This is easily verified from $n = 64$ to 192.

The same pattern of depth-broadening invariance is also seen in LREF-1 in the presence of edges. Figure 3 shows the reconstruction of a truncated exponential profile over a range of depths in the model coordinate at the regularization level $\lambda_0 = 0.01$. Because of the logarithmic abscissa, the profile appears slightly distorted. The value of β was scaled constant on the logarithmic scale: β here is computed as a normalized multiple of the reciprocal profile width, per $\beta = m/\Delta$ (where m is a real-valued multiplier that amounts to an ab-

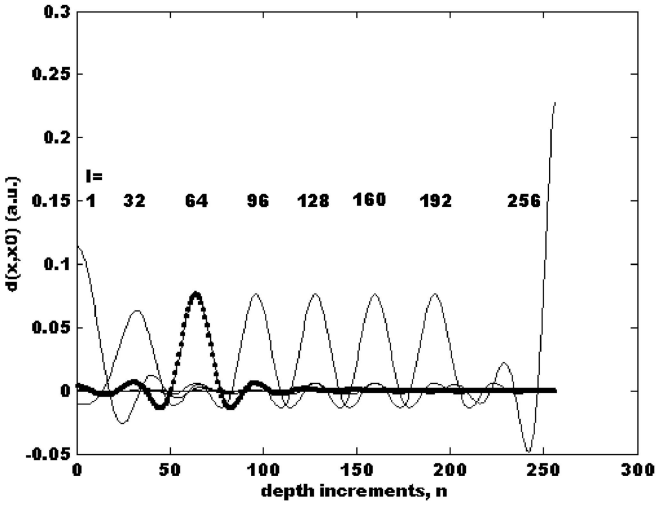

FIGURE 2 Samples of the resolving kernel $\delta(x, x_0)$ over depth coordinate (n), showing reconstruction of delta-function sources placed at depth positions indexed 'i' in the model space. Source at $i = 64$ is highlighted (.-.-.-)

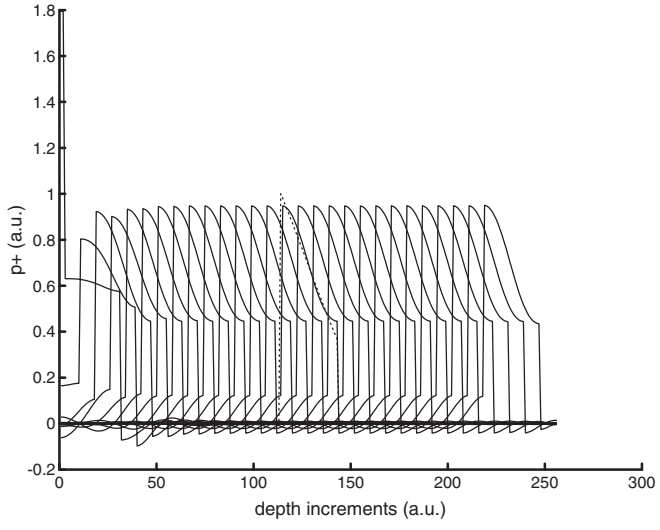

FIGURE 3 LREF-1 reconstruction of a truncated exponential placed at increasing depth from the sample surface. The theoretical profile $p_2(x - x_n)$ is shown highlighted at a depth of $n = 128$ increments (.-.-.-)

sorbance: $m = \beta\Delta$ and $\Delta = x_{n+\Delta} - x_n$). Theory is shown super-imposed as the dotted (black) trace in the middle of the depth space, to give a guide as to the degree of reconstruction fidelity.

3.2 *Choice of the regularization level λ_0*

The parameter λ in (15) determines the relative weighting between the χ error residual ((7) and the side constraint (8)). The discrepancy principle [41] suggests that λ should be set so that $\lambda \approx \chi$. This expression is extended to the following:

$$\lambda = h_p \sigma_r \sqrt{N}, \tag{35}$$

where h_p is the peak signal level in the data and σ_r is the relative noise level in the data (referenced to a full-scale value of unity). Equation (35) assumes that the data residuals give a good estimate of the random error in the data when λ is near the optimum value. From this we can identify a base regularization level, $\lambda_0 = \sigma_r$, e.g. at which profile reconstructions are stable, for a given error in the data.

The L curve [42] is another well-known criterion for determining an optimum value of λ in Nth-order Tikhonov regularization. This method prepares a plot of $\log\|\mathbf{L} \times \mathbf{p}\|$ versus $\log \|\chi\|$ over multiple values of λ, in which a corner feature appears when errors are small. The corner feature represents the balance between the chi error and the side constraint. The value of λ occurring at the corner may be considered the best compromise to ensure stability in $\mathbf{p}^+$ without excessive filtering (bias) by the side constraint. It is also known that the value of λ predicted by the discrepancy principle (35) is close to the corner value of the L curve, typically [23, 42].

The LREF-1 algorithm was tested for conformity to the L curve, by adding random errors to the data at relative level σ_r, and performing inversions on a truncated exponential profile with (conditions as in Fig. 2): depth 74, width, $\Delta = 64$ and decay coefficient, $\beta = 1/\Delta$ in the model space units. The resulting L curve yielded corner values within a factor of 1.5–2 of that predicted by the discrepancy principle. This was deemed close enough that (35) could be invoked to stably invert profiles at data noise levels σ_r.

It was also found by numerical computations that the reconstruction errors were only weakly dependent on the value of λ_0 in the range of 0.001–0.01.

3.3 *Depth-profile reconstructions*

LREF-1 was tested on a set of profiles that have been a classical challenge to Tikhonov reconstruction methods [5–7, 25]. These profiles, summarized by (29a)–(29c), have edge positions at the interfaces x_i. The LREF-1 algorithm places marker entries (unit values) in the **v** vector of (12) at the corresponding 'i' positions (or the best approximations thereto). In the first set of calculations presented here, the depth coordinates for forward and inverse theories had identical discretization, so that the **v** entries were specified exactly. Stability in the presence of errors in the estimate interface positions is demonstrated in Sect. 3.5. Since broadening is invariant with depth over the model coordinate, n (cf. (33)), the leading depth x_1 is fixed and the other profile parameters are varied.

Figure 4 gives the LREF-1 reconstruction of a flat-top or box profile, at fixed x_1 but variable profile width $\Delta \equiv (x_2 - x_1)$. The classical $n = 1$-order Tikhonov regularization is shown for reference in Fig. 5. Both reconstructions are run at a regularization level λ_0 of 0.01, which indicates that the reconstructed profiles are stable at an experimental noise level of 1% of full scale in the data.

Both algorithms show an effect on the box width Δ. When Δ is comparable to Δ_δ, the half-width of $\delta(x, x_0)$, which measures intrinsic resolution limits (Fig. 2), TR-1 returns a profile dominated by this spread. Under the same conditions, LREF-1 returns a box-shaped profile because of the boundary constraints introduced by the edge field, but an error in the reconstruction is nonetheless introduced. As Δ increases to

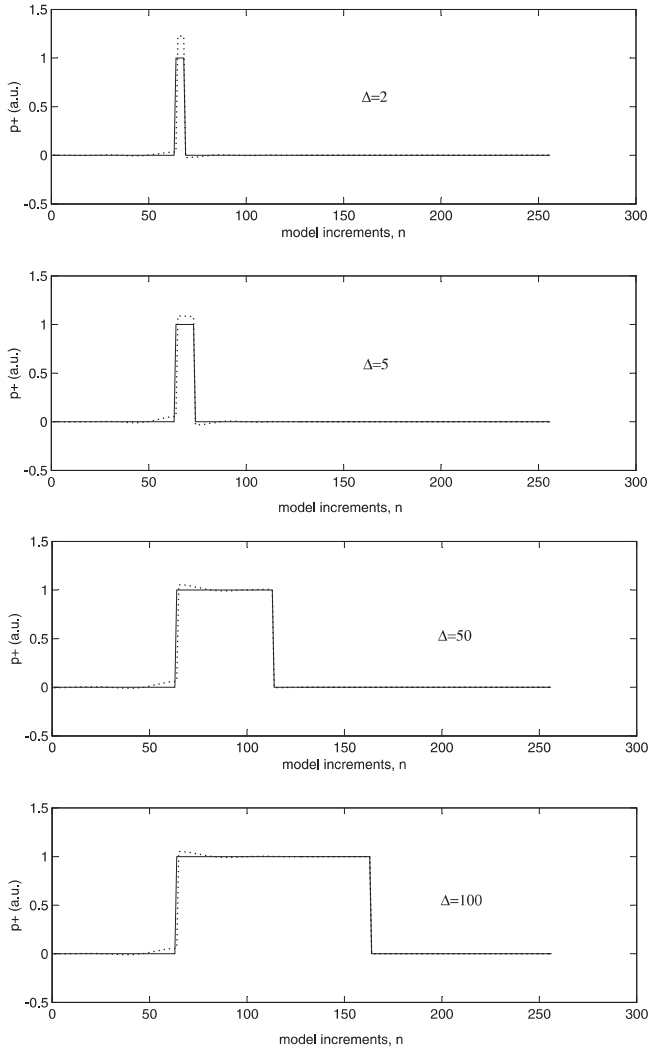

FIGURE 4 Reconstruction of a flat-top profile by LREF-1 at $\boldsymbol{\lambda}_0 = 0.01$ and constant depth ($x_1 = 64$) for increasing value of the width parameter Δ. *Solid line* (————): theory, $p_2(x)$; *dashed line* (.-.-.-.-): $\mathbf{p}^+$

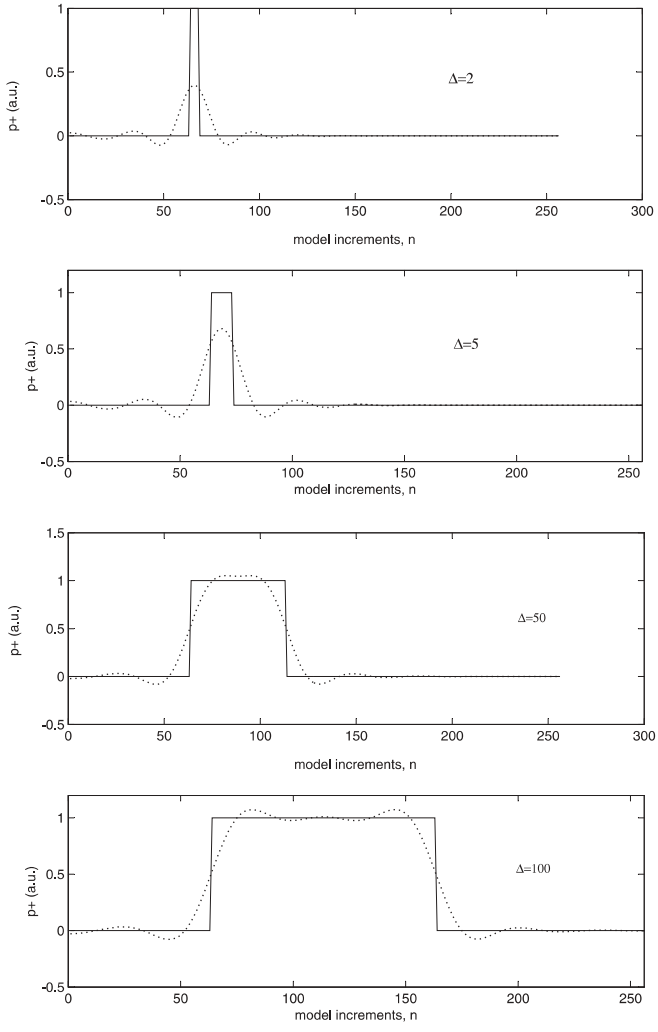

FIGURE 5 Reconstruction of a flat-top profile by TR-1 at $\boldsymbol{\lambda}_0 = 0.01$ and constant depth ($x_1 = 64$) for increasing value of the width parameter Δ. *Solid line* (————): theory, $p_2(x)$; *dashed line* (.-.-.-.-): $\mathbf{p}^+$

a large value relative to the width of $\delta(x, x_0)$, LREF-1 profiles show minor errors at the profile edges but, otherwise, excellent reconstructive fidelity. TR-1 shows the classical edge smoothing and oscillations seen in prior work [5–7, 25].

Similar effects appear in reconstructions on truncated exponentials (Figs. 6 and 7). Again (Fig. 6), when Δ is close to Δ_δ, the half-width of $\delta(x, x_0)$, LREF-1 returns a box-shaped estimate of the profile, but when $\Delta > \Delta_\delta$ (approximately) a smooth continuous profile is fitted between the boundaries. The corresponding TR-1 computations (Fig. 7) show substantial edge broadening, even when $\Delta >> \Delta_\delta$. Error analyses, presented below, show that the root-mean-square (rms) deviation from theory approaches a constant value at large enough Δ.

The performance of LREF-1 on complex multi-interface profiles shows the full advantages of the edge-field formulation. Figure 8 shows the reconstruction of a two-component exponential profile with weighting between sections. In Fig. 8a all model interfaces are marked in the edge-field vector, **v**. Figure 8b shows the effect of removing the edge-field marker in **v** at the middle interface. A classic pattern of broadening and oscillation shows up in the vicinity of the unmarked edge, as would be expected for unconstrained Tikhonov regularization (Fig. 8c).

Another advantage of LREF-1 seen in this example is that the pattern of reconstruction errors seen in each segmented zone of the profile is independent of any fit errors appearing in other zones. This is an important feature of the edge-field operator, which has been shown in previous work. By contrast, with TR-1 (TR-*n* generally) errors introduced into one region of the model space are globally distributed, which is consistent with the fitting of a single constant (in general, derivative) over the entire depth space by TR. LREF-1, by contrast, allows regularization to occur as a set of box-like segmented regions that are bounded by the edge-field markers.

Notwithstanding Fig. 8, there are cases where an edge field of the form of (13) may not be appropriate. Figure 9 gives the reconstruction of a two-layer exponential profile where there is no discontinuity in amplitude at the interface between layers, but where the decay coefficient (β) changes. In Fig. 9a all interfaces in the model depth are marked in **v** while, in Fig. 9b, the edge-field marker on the middle inter-

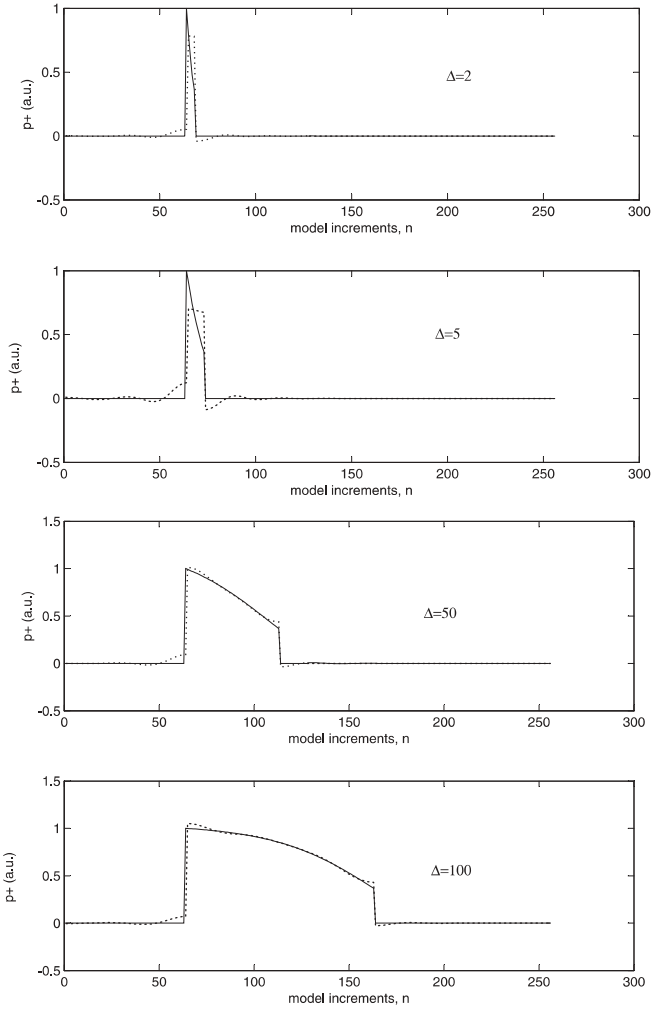

FIGURE 6 Reconstruction of a truncated exponential profile with $\beta = 1/\Delta$ by LREF-1 at $\lambda_0 = 0.01$ and constant depth ($x_1 = 64$) for increasing value of the width parameter Δ. *Solid line* (———): theory, $p_2(x)$; *dashed line* (.-.-.-.-): $\mathbf{p}^+$

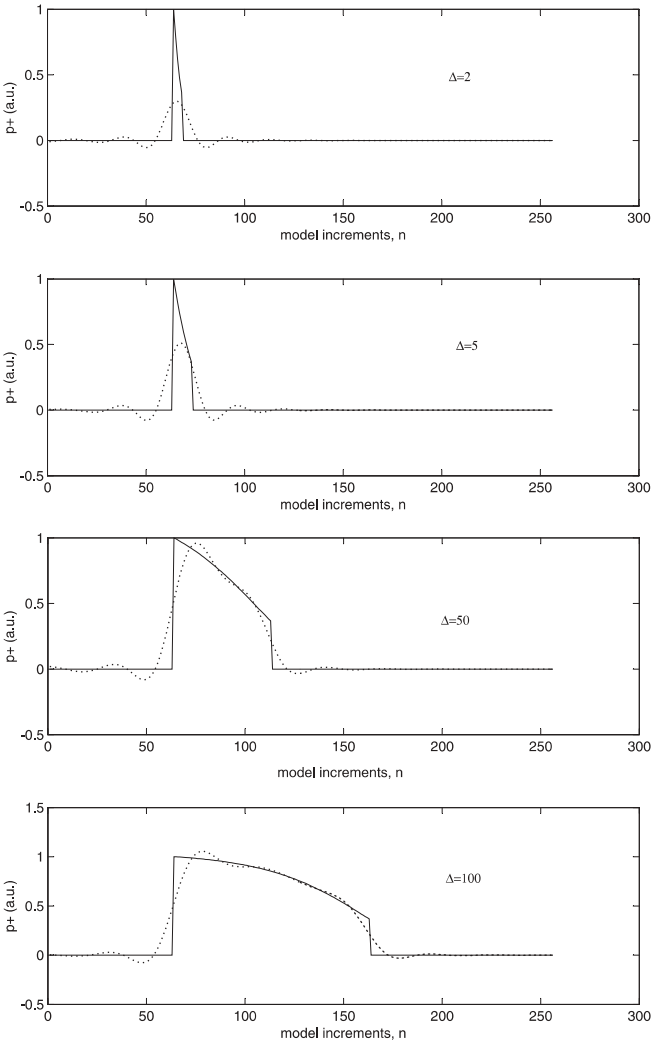

FIGURE 7 Reconstruction of a truncated exponential profile with $\beta = 1/\Delta$ by TR-1 at $\lambda_0 = 0.01$ and constant depth ($x_1 = 64$) for increasing value of the width parameter Δ. *Solid line* (———): theory, $p_2(x)$; *dashed line* (.-.-.-.-): $\mathbf{p}^+$

face is omitted. It can be seen that the effect of the edge-field marker is to introduce an amplitude discontinuity (a 'glitch') at each interface, even where none exists, as in the case of the middle interface. The height of the 'glitch' diminishes with regularization level, λ_0, but only slowly. Here, it can be seen in retrospect why the original choice of $n = 1$ regularization was appropriate to reconstruct an edge. The choice of $\mathbf{L}_1$ allows the free fitting of an amplitude discontinuity at the interface, as is typical of an edge. However, when the interface discontinuity involves a change in slope, a better choice of regularization functional at the middle interface would be one that allows the first derivative of $\mathbf{p}^+$ (instead of the amplitude) to be discontinuous. This would mean a substitution of the $\mathbf{L}_1$ functional by an $\mathbf{L}_2$ difference operator in (13).

Finally, a comparison was made of the LREF-1 algorithm against a reference TR-1 computation, in which prior information was introduced into the vector $\mathbf{p}_0$ (28). A flat-top prior profile was set in $\mathbf{p}_0$, having the same dimensions as a truncated exponential to be reconstructed. With regularization levels set at $\lambda_0 = 0.005 - 0.01$, inversion of the data profiles resulted in significant distortions in $\mathbf{p}^+$, especially near the

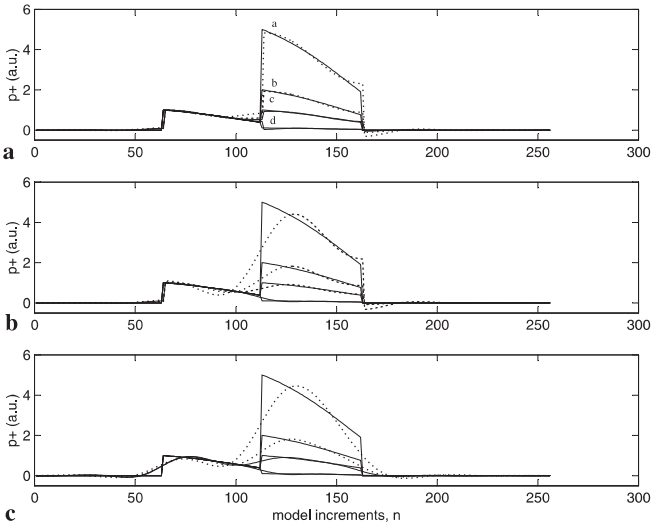

FIGURE 8 LREF-1 reconstructions of a two-layer profile at $\lambda_0 = 0.01$ with exponentially decaying contrast in each layer, and non-unity weighting on the second layer with **a** all model interfaces marked; **b** middle interface unmarked; **c** all interfaces unmarked (TR-1). Weights (a–d) applied to the second layer were: a:5; b:2; c:1; d:0.1, with unity weighting on the first layer

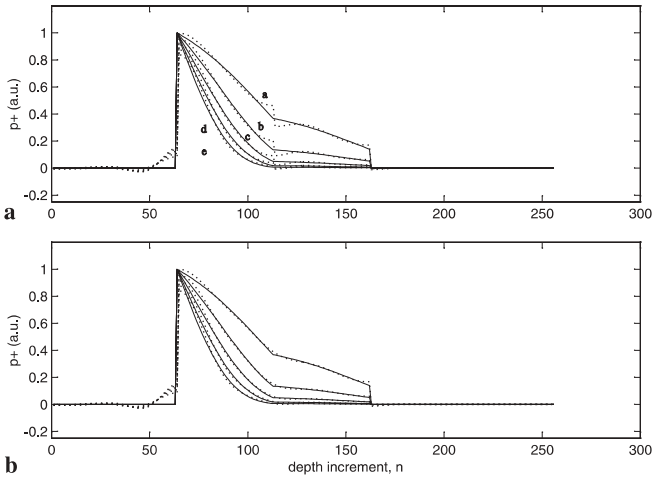

FIGURE 9 LREF-1 reconstructions of a two-layer profile at $\boldsymbol{\lambda}_0 = 0.01$ with exponentially decaying contrast in each layer, and non-unity weighting on the second layer with: **a** all model interfaces marked; **b** middle interface unmarked; (a–e) are values of the decay-constant coefficients applied to the first layer (in units of $1/\Delta_1$), namely a:1; b:2; c:3; d:4; e:5

profile edges, where the box structure of the prior term tended to dominate in preference to the exponential decay.

3.4 *Effect of the edge field on the GSVD analysis*

At this point, the effect of the edge field on the structure of the basis functions returned by the GSVD is considered. In (16), the GSVD accounts for the depth information in **G** and **L** by means of a set of basis vectors contained in the operator $\mathbf{W} \equiv (\mathbf{X}^{\mathrm{T}})^{-1}$ (where the change of notation is introduced for convenience). The column vectors in **W**, while not strictly orthogonal [23], are linearly independent and reconstruct the spatial information $\mathbf{p}^{+}$. The solution profile computed by (15) may be expressed as a superposition of column vectors in **W** according to the expression [23]:

$$p^{+} = \sum_{i=1}^{N} A_i W_i, \tag{36a}$$

where

$$A_i = \left(\frac{F_i}{a_i}\right)\left(\mathbf{U}_i^{\mathrm{T}} \times \mathbf{h}\right). \tag{36b}$$

Note that $F_i/a_i = 1$ for $i >$ Q along the diagonal of the matrices **F** and $(\mathbf{a}^{-1})^{\mathrm{T}}$; $\mathbf{U}_i^{\mathrm{T}}$ is the transpose of the ith column vector of **U** (cf. (16)).

In this depth reconstruction, the column vectors in **W** function analogously to the right singular vectors, **V**, in the SVD ((4a) and (4b)). In SVD computations the $\mathbf{V}_i$ (right) singular (column) vectors are ordered, in general, according to an increasing number of zero crossings in the depth dependence, as the index, 'i', increases. They function analogously in the depth reconstruction to a set of sinusoids in a Fourier superposition. In the case of the $\mathbf{W}_i$ columns returned by Matlab's GSVD procedure [38], increasing 'i' indexes a decreasing number of zero crossings. The computations used in this work reverse this indexing for consistency with the ordering used by the SVD [21, 23].

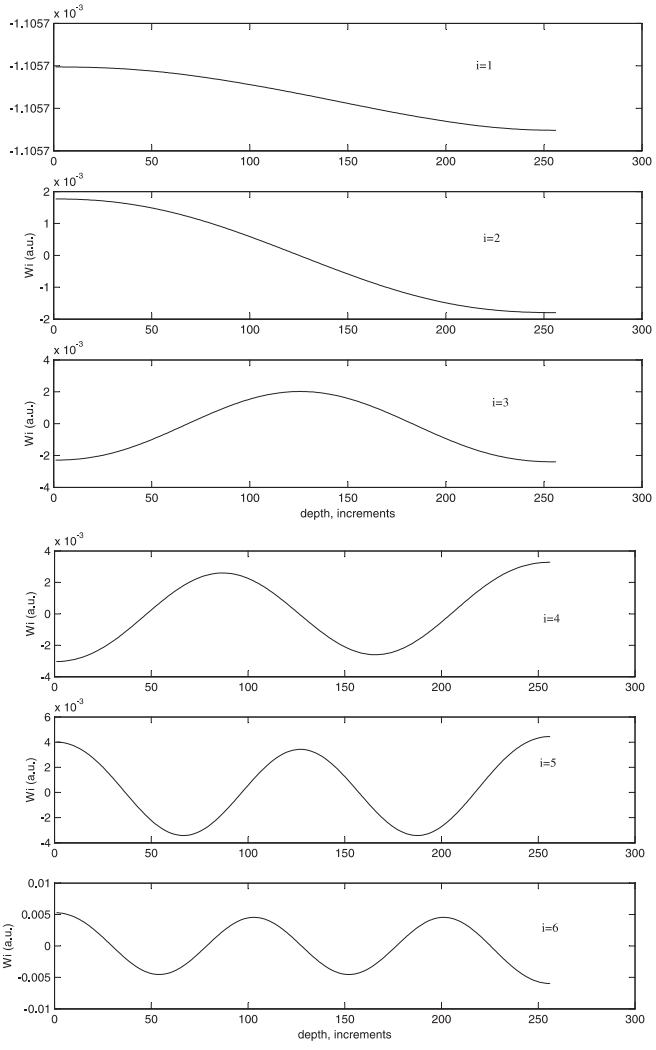

FIGURE 10 Display of six lowest-ordered column vectors of the depth-reconstruction set **W** returned by the GSVD, for input arguments $\{\mathbf{G}, \mathbf{L}_1\}$

Figure 10 shows the first six 'i' (reverse-ordered) indices of the **W** columns for the **G** basis set (kernel) computed in (16a) and (16b), regularized against the $\mathbf{L}_1$ operator with no edge field. These vectors are continuous and quasi-sinusoidal, with a frequency-like argument that increases as 'i'. When edge constraints are imposed on $\mathbf{L}_1$ through the edge field (13), discontinuities appear in the $\mathbf{W}_i$ at the model index positions corresponding to the edge-field markers (note that the marker positions are set at model coordinates (n) of 64 and 163, in this example) (Fig. 11). The presence of these discontinuities allows segmentation of the model fitting into independent zones. In particular, the lowest-ordered singular vectors, which will tend to dominate an ill-posed problem such as this one, resemble a set of box structures. This explains why box-like profiles are easiest for the LREF-1 algorithm to reconstruct: they represent the lowest order of terms in the series in (36a). Here, LREF-1 is implementing TR-1 regularization ($\mathbf{p}^{+} =$ const.) over multiple segmented zones where the constant is allowed to vary locally and independently of other zones.

Based on the effect of the edge field on the $\mathbf{W}_i$ reconstruction set, and the results of Figs. 4 and 6, which show a nearly

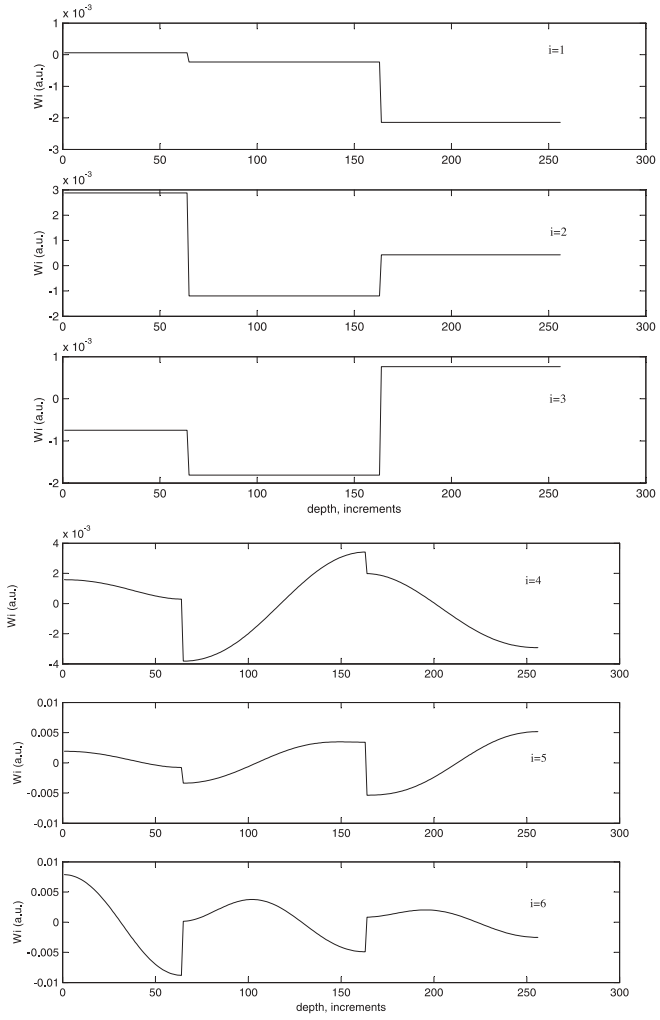

FIGURE 11 Display of six lowest-ordered column vectors of the depth-reconstruction set **W** returned by the GSVD, for input arguments $\{\mathbf{G}, \mathbf{M}_1\}$

constant reconstruction error when $\Delta > \Delta_\delta$, we can estimate the number of independent bounded depth zones into which the model space can be partitioned as $N_z \approx N_r/\Delta_\delta$. This has not been directly tested here but is consistent with the principles of the edge-field operator as seen in [33], and in the above demonstration.

3.5 *Stability tests*

A key requirement of any inversion algorithm is stability in the presence of small errors in discretization and in the prior information.

A key test of stability was to examine the effects of systematic estimation errors on the interface positions in the edge field. If the inverse solution is stable, $\mathbf{p}^+$ should not show catastrophic sensitivity to small errors in the **v** entries.

Figure 12 examines the effects of errors in the marker positions on the reconstruction of a truncated exponential profile. Here, the profile has leading depth $x_1 = 6.84\ \mu$m, width $\Delta = 29.3\ \mu$m, back-interface depth $x_2 = 36.1\ \mu$m and unit absorbance, m, over the layer width ($\beta = m/\Delta$ with $m = 1$). Errors of ± 5 model increments were applied simultaneously at both interfaces, with the same sign and magnitude as indicated in the figure caption. A random error level $\sigma_r = 0.01$ (1% of full scale) was introduced into the data.

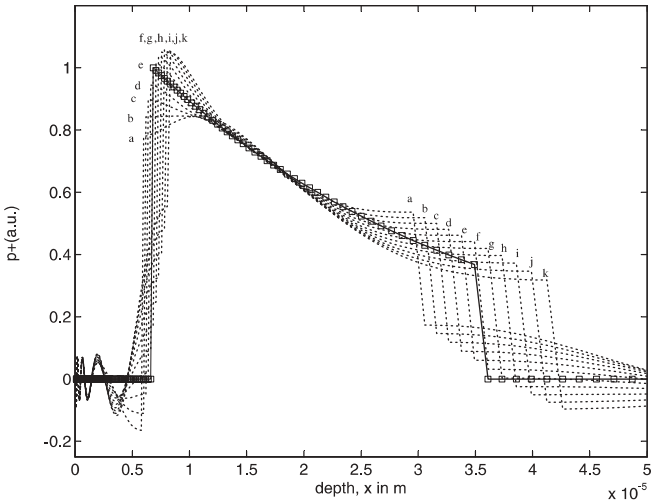

FIGURE 12 Effect of interface estimate errors on the analysis of a typical thin layer; squares: theory; .-.-.-, reconstructions with errors in assumed interface positions. Profiles (a, b, c, d, e) simultaneously apply marker entry errors of $(-5, -4, -3, -2, -1)$ model increments to front and rear interfaces; profiles (f, g, h, i, j) respectively apply errors of (1, 2, 3, 4, 5) model increments

As Fig. 12 shows, errors at a level of close to 15% at the rear interface have the effect of shortening or lengthening the fitted profile by the estimated amount, but without the introduction of catastrophic instability. When x_2 is underestimated (profiles a–e), the induced deviation of $\mathbf{p}^+$ from $p_2(x)$ is no more that 10% over the bounds of the assumed profile. When x_2 is overestimated (profiles f–j), even smaller errors are introduced. The fit in $\mathbf{p}^+$ tends to extrapolate the fitted exponential past the back interface, terminating it at the (assumed) marker position. A similar pattern of stability appears at the front interface, although here the reconstruction shows more sensitivity to the errors in the interface position.

The practical consequences are that a stable meaningful depth profile should continue to be recovered by LREF-1 even in the presence of substantial errors ($\pm 15\%$–20%) on the estimate interface positions in **v**.

The next question raised by this result is whether the residual error is sufficiently sensitive to the interface locations that the correct values may be determined by minimizing χ with respect to the entries in **v**. This is examined in Fig. 13, which shows a plot of χ(rms) (7) versus the error in the interface estimate in model increments. This effect was independently studied at the front and rear interfaces of the model. The errors were found to be additive. The χ error is reported as a fraction of the full-scale data signal (to give an estimate of the sensitivity of the data to interface displacement). Within the error range of ± 5 model increments at the front surface, χ produced a variation of 0.025% of the full-scale signal level in the data. At the rear interface, the corresponding figure was 0.005%. These error profiles were computed from the average of five data (**h**) sets, containing independent random errors at a level of 1% of full scale (and with $\lambda_0 = \sigma_r = 0.01$). The minima in χ are both broad and slightly displaced from zero, the latter being the probable result of error introduced by the regularization. Because of the ill-posed nature of the

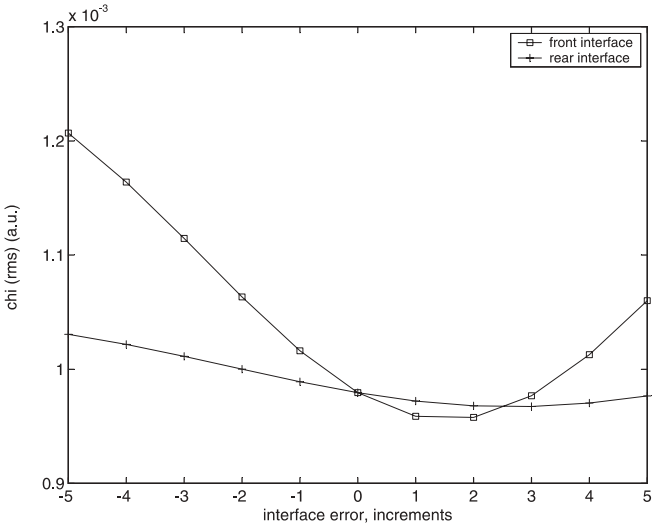

FIGURE 13 Chi residuals obtained as a function of displacement of front and rear interfaces away from the exact ('0') position

problem, the residual error is classically insensitive to the interface positions. The profile fit at the front interface is more sensitive to interface estimate errors than the back, the probable reason being that the latter is attenuated by a factor of 2.5 times relative to the front, through the exponential decay relationship. Attenuation and delocalization of signal energy from $G(x, x_0, t)$ at the deeper edge should not account for a reduced edge sensitivity effect on χ, because here the model basis, **G**, should compensate for both depth attenuation and spatial resolution in $\mathbf{p}^+$ through its non-uniform structure. The computation of error characteristics based on a small number of replicated data sets may possibly account for any additional effects of χ sensitivity between the front and rear interfaces. The practical consequences for using χ minimization in a practical reconstruction are discussed below.

3.6 *Error evaluation*

The final issue addressed was the error evaluation of the algorithm in reconstructing optical absorption between edge boundaries as a function of depth. A root-mean-square (rms) error was computed between the reconstruction and theory:

$$\varepsilon = \left\| p^+ - p_2(x) \right\| / \max\left(p_2(x)\right) \qquad (x_1 < x < x_2), \quad (37)$$

for the profile $p_2(x)$ being a truncated exponential (29b). This error is calculated inside the boundaries of the defined profile. This is repeated in the presence and absence of the edge field. The error is normalized to the maximum contrast level in $p_2(x)$ (unity).

We have already established in Figs. 2 and 3 that, provided all distances are defined over the index n (cf. (33)), broadening in the depth profile, $\mathbf{p}^+$, is not affected by the leading depth x_1 because the half-width of the resolving kernel, Δ_q, is invariant over this depth space. The remaining variables that affect broadening are β and Δ, more specifically Δ/Δ_δ, since it is the profile width relative to the base-broadening distance that is significant. To this end, an inspection of the form of $\delta(x, x_0)$ (Fig. 3) shows that at $\lambda_0 = 0.005$ the distance from the peak to the second zero crossing is 27 model increments.

Figure 14a and b show error contours $\varepsilon(\beta\Delta, \Delta/\Delta_\delta)$ for the reconstruction of a truncated absorption profile displaced at $x_1 = 64$ model increments into the depth space as the layer absorbance, $\beta\Delta$, varies from a value of 0 (the flat-top condition) to the condition $\beta\Delta = 3$. Because of the non-uniform structure of the depth space, errors are computed for variable layer absorbance $\beta\Delta$ in preference to the decay coefficient, β, to describe these effects. The relative profile width is varied from $\Delta/\Delta_\delta = 0$ to 7. The contour is masked out in black where the reconstruction error ε exceeds 10% of full scale. Reconstruc-

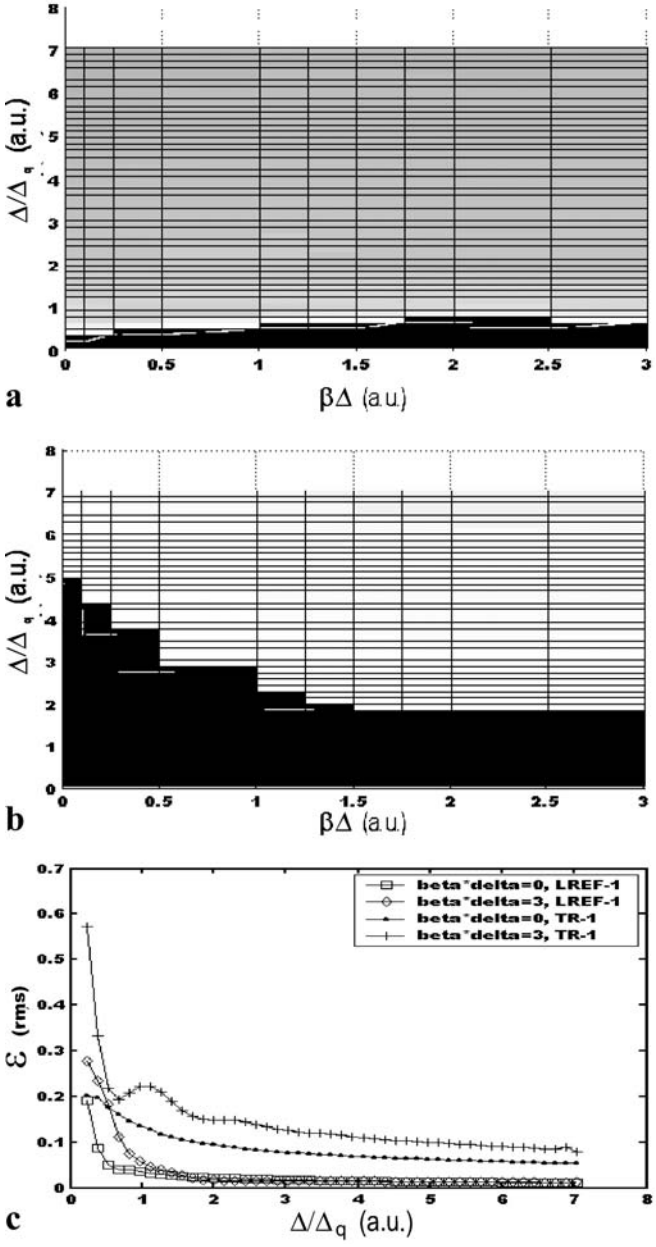

FIGURE 14 Error contours (90° view) showing χ plotted as a function of the layer absorbance $\beta\Delta$ and the normalized width Δ/Δ_q. The region masked off in black shows conditions for which the profile-fitting error exceeds 10% in (37): **a** LREF-1; **b** TR-1; **c** slice sections of contours in **a** and **b** for indicated cases; $\boldsymbol{\lambda}_0 = 0.005$ throughout

tion errors above this level may be considered unacceptable. Figure 14c shows individual line plots of the error residual for $\beta\Delta = 0$ and $\beta\Delta = 3$.

The line plots in Fig. 14c show the following common features for LREF-1 and TR-1. First, at small Δ such that $\Delta < \Delta_\delta$, ε decreases rapidly for increasing Δ. This is not surprising because Δ_δ limits the depth resolution for TR-1, and for LREF-1 inside the edge boundaries set in **v**. Second, for $\Delta >> \Delta_\delta$, ε flattens to a nearly constant value, ε_∞, that is independent of β. This is a classic effect seen elsewhere [25]. Between these two zones of rapidly decreasing and constant error, there is a turning point value of Δ/Δ_δ, which marks the transition. This turning point ratio lies in the range from approximately 0.6 to 1.6, and is dependent on β.

From this point, we can also see some obvious differences between the error profiles (ε versus Δ/Δ_δ). First, the errors in LREF-1 are consistently smaller than TR-1 over the entire parameter space: ε_∞ obtained for TR-1 is a factor of 4.5 larger than for LREF-1. This is consistent with the reconstruction examples presented in Figs. 4–7. Below $\Delta/\Delta_q = 2$, the error profiles obtained for LREF-1 are continuously decreasing, and the case $\beta\Delta = 0$ tends to give the smallest error at small Δ. This is consistent with this algorithm's box-like zero-order estimate of the profile features. The TR-1 error profile is continuously decreasing at large $\beta\Delta$, and has a smaller magnitude at large $\beta\Delta$ than for $\beta\Delta = 0$. In this latter case, a secondary maximum appears at $\Delta/\Delta_q \sim 1$. This feature is consistent with the resolution problems seen by Tikhonov methods in reconstructing box-like objects [6, 7, 21, 23, 33].

The error contours in Fig. 14a and b show a dramatic improvement in overall performance for LREF-1 over TR-1. At large Δ the ε_∞ improvement is nearly a factor of 5 while, in the intermediate zones, the improvement is as large as 6–8 times. The total size of the excluded zone of relative reconstruction error greater than 10% is dramatically larger for TR-1 than for LREF-1.

The broad features of this analysis are consistent with earlier work [25]; however, some complicating features are present here. First, the kernel derived in (30) requires modification for comparison to a specific instrumental technique such as photothermal radiometry [6–8], although the general behavior of the algorithm remains applicable. Second, this work uses a non-uniform depth coordinate in which the effect of profile depth, x_1, is removed as a broadening factor in the analysis. Third, $n = 1$ Tikhonov regularization is examined as the depth-continuous reference (as opposed to the truncated SVD of past work). In practice, the TR-1 reconstruction shows a somewhat improved resolution over TR-0, so the error improvement offered by the edge-field analysis estimated here is conservative.

4 Discussion

This algorithm, so far developed in theory, remains to be evaluated for experimental measurements. The availability of estimates of interface positions to within 3–10 μm (of the thermal depth space) is feasible in many situations. In the type-I photothermal problem, it suffices to scale the measured interface positions, x_i, by the sample's thermal diffusivity per $x_i/\sqrt{\alpha}$. This is very straightforward in media such as tissues, which are dominated by the thermal properties of water. The stability of the methodology [6–8] in the presence of typical experimental errors shows promise for practical recovery problems.

An evaluation of the algorithm on laboratory data must contend with issues such as the effects of common bias errors in the experiment, and geometric constraints that may restrict the depth space of the problem. Such an undertaking is left to future work. Uniform depth spaces are more practical with methods that lack the optimally wide bandwidth of the present simulation. However, the underlying heat principles governing broadening of the depth profile will be the same there as here. In methods such as mirage-effect spectrometry [43, 44], where at least one major interface is present between the sample surface and a fluid-deflection medium, the improvement in depth resolution furnished by the use of an edge field should be significant.

New prospects potentially open up for this algorithm in photothermal tissue diagnostics. Infrared photothermal radiometry has been of special interest in laser-based tissue therapies because of its unique potential, based on a solution to the type-I inverse problem, for profiling the absolute subsurface temperature of a tissue under pulsed laser irradiation [6–8]. However, the broadening of conventional Tikhonov reconstructions has made accurate temperature measurements in the dermal layers all but impossible for the general case [25]. Recently, attention has turned to optical coherence tomography (OCT)/low-coherence optical reflectometry [30, 31] as an alternative method of tissue-depth profilometry. This technique uses elastic scattering contrast in tissues to deliver a density profile with a resolution of $\sim 10\,\mu$m, without the ill posedness of photothermal techniques but also without the temperature and optical absorption contrast. Both photothermal radiometry and OCT [8, 31] have been developed for in situ monitoring. Potentially, the use of edge-field regularization incorporating OCT to identify interface locations, and photothermal profilometry for temperature mapping, may provide possible compensation for the limitations seen in the past with classical Tikhonov methods.

Another extension of the edge-field concept that remains to be explored in tissue (skin) diagnostics lies in three-dimensional photothermal reconstruction problems of the type-I formulation [44]. The latter have been used to map temperature and optical absorption in blood vasculature, and to map the position of individual large blood vessels in the dermis (~ 0.05–2.5 mm). Modifications of the edge-field operator may allow complex surface constraints to be imposed on three-dimensional images [33], and potentially to improve imaging accuracy dramatically. The accurate measurement of optical absorption spectra of blood flowing in individual large blood vessels may also become possible.

Further possibilities also exist for extending the edge-field regularization to the type-II inverse problem. In a solid that is surface-heated by an impulse, the recorded photothermal signal may be expressed as the sum of reflected and transmitted thermal components that are spatially displaced and time-delayed images of the surface-generated temperature field as it would propagate in a homogeneous infinite medium [14]. For heat diffusion accessing 'n' layers in the model space, a lumped reflection coefficient may be derived that accounts

for the yield of energy returned to the surface. This coefficient weights the amplitude of an image field accounting for heat diffusion over a fixed-length optical path. A recent model [14] of the type-II problem shows how the surface temperature may be expressed as the summation of a set of image fields (Green's functions for heat conduction) weighted by lumped reflection coefficients, A_n, from which the interfacial thermal effusivity ratio with depth may be computed. In this formulation, the A_n directly access defined depths in the model space $x_n = n\Delta x$ (with Δx the (uniform) model layer thickness), and are the primary set of variables inverted from the data. Since the Tikhonov regularization applies as a stabilizer, and x_n is well defined, the edge field may be used to mark the depth locations where discontinuities are known to occur.

Another issue of practical importance that arises is the blind detection of interfaces in the model space [33–35]. We consider the case of a material having a known number of interfaces but of unknown location. Early vision problems have shown some success in determining both the number and locations of interfaces in a reconstructed image on a blind basis [33–35]. The severely ill-posed character of the photothermal problem more or less ensures that any data residuals will have a very weak sensitivity to interface locations, as confirmed in the study of Fig. 13. Nonetheless, experimental and theoretical work [43, 44] has confirmed that small variations in the data residuals, up to two orders of magnitude smaller than the random error levels in the data, may still contain sufficient information to guide the correct location of an interface. However, the success of such a scheme requires high-quality data with very low levels of bias errors. Future work will provide an assessment of this problem based on experimental data.

5 Conclusion

Edge-field regularization provides a possible route for compensation of the depth-resolution limits of classical Tikhonov regularization. The edge field is used to mark the location of known interfaces in the model space, as furnished by prior knowledge or alternate detection methods. The edge-field formulation implements n^{th}-order Tikhonov regularization in windowed segments of the model space, where the errors in regularization are restricted to within the windowed zones.

ACKNOWLEDGEMENTS The author would like to thank the Natural Sciences and Engineering Research Council of Canada (NSERC) for their support of this work

REFERENCES

1 M.A. Afromowitz, P. Yeh, S. Yee: J. Appl. Phys. **48**, 209 (1977)
2 H.J. Vidberg, J. Jaarinen, D.O. Riska: Can. J. Phys. **64**, 1178 (1986)
3 A. Harata, T. Sawada: J. Appl. Phys. **65**, 959 (1989)
4 A. Mandelis, E. Schoubs, S.B. Peralta, J. Thoen: J. Appl. Phys. **70**, 1771 (1991)
5 J.F. Power, M.C. Prystay: Appl. Spectrosc. **49**, 725 (1995)
6 T.E. Milner, D.M. Goodman, B.S. Tanenbaum, J.S. Nelson: JOSA **12**, 1479 (1995)
7 U.S. Sathyam, S.A. Prahl: J. Biomed. Opt. **2**, 251 (1997)
8 S.L. Jacques, J.S. Nelson, W.H. Wright, T.E. Milner: Appl. Opt. **32**, 2439 (1993)
9 T.E. Milner, D. J Smithies, D.M. Goodman, A. Lau, J.S. Nelson: Appl. Opt. **35**, 4379 (1996)
10 J.F. McClelland, R.L. Jones, S. Bajic, J.F. Power: Mikrochim. Acta [Suppl.] **14**, 613 (1997)
11 T.T. Lan, U. Seidel, H.G. Walther: J. Appl. Phys. **77**, 4739 (1995)
12 R. Li Voti, G.L. Liakhou, S. Paoloni, E. Scotto, C. Sibilia, M. Bertolotti: 'Theory of photothermal depth profiling in time domain'. In: Photoacoustic and Photothermal Phenomena: Proceedings of Tenth International Conference (AIP Conf. Proc. 463), ed. by F. Scudieri, M. Bertolotti (AIP, Woodbury, New York 1999) pp 37–39
13 C. Glorieux, R. Li Voti, J. Thoen, M. Bertolotti, C. Sibilia: J. Appl. Phys. **85**, 7059 (1999)
14 J.F. Power, J. Karanicolas, S.W. Fu: Appl. Phys. B **71**, 57 (2000)
15 A. Mandelis: *Diffusion Wave Fields: Mathematical Models and Green Functions* (Springer, New York 2001)
16 L. Nicolaides, A. Mandelis: J. Appl. Phys. **90**, 1255 (2001)
17 U. Seidel, T.T. Lan, H.G. Walther, B. Schmitz, J. Geerkens, G. Goch: Opt. Eng. **36**, 376 (1997)
18 T.T.N. Lan, H.G. Walther, D.T. Son, P. Wiesner: Haerterei Tech. Mitt. **52**, 241 (1997)
19 C. Glorieux, J. Thoen, J. Fivez: J. Appl. Phys. **73**, 684 (1993)
20 H. Machlab, W.A. McGahan, J.A. Woollam, K. Cole: Thin Solid Films **224**, 22 (1993)
21 J.F. Power: Rev. Sci. Instrum. **73**(12), 4057 (2002)
22 J.F. Power: 'A Survey of Current Issues in Inverse Problem Theory as Applied to Thermal Wave Imaging'. In: Photoacoustic and Photothermal Phenomena: Proceedings of Tenth International Conference (AIP Conf. Proc. 463), ed. by F. Scudieri, M. Bertolotti (AIP, Woodbury, New York 1999) pp 3–7
23 P.C. Hansen: Inverse Probl. **8**, 849 (1992)
24 M. Bertero, C. De Mol, E.R. Pike: Inverse Probl. **1**, 301 (1985)
25 D.J. Smithies, T.E. Milner, B.S. Tanenbaum, D.M. Goodman, J.S. Nelson: Phys. Med. Biol. **43**, 2452 (1998)
26 S. Ekgasit, H. Ishida: Appl. Spectrosc. **50**, 1187 (1996)
27 J.F. Power, S.W. Fu: Appl. Spectrosc. **53**, 1507 (1999)
28 J.F. Power, S.W. Fu: Apparatus and method for light profile microscopy. US Patent Application (pending)
29 A.A. Karabutov, N.B. Podymova, V.S. Letokhov: Appl. Phys. B **63**, 545 (1996)
30 D. Huang, E.A. Swanson, C.P. Lin, J.S. Schuman, W.G. Stinson, W. Chang, M.R. Hee, T. Flotte, K. Gregory, C. Puliafato, J.G. Fujimoto: Science **254**, 1178 (1991)
31 D.J. Smithies, T. Lindmo, Z. Chen, J.S. Nelson, T.E. Milner: Phys. Med. Biol. **43**, 3025 (1998)
32 A. Diaspro (ed.): *Confocal and Two Photon Microscopy: Foundation, Applications and Advances* (Wiley-Liss, New York 2002)
33 D. Terzopolous: IEEE Trans. Pattern Anal. Mach. Intell. **8**, 413 (1986)
34 P. Lalanne, D. Prevost, P. Chavel: Appl. Opt. **40**, 3861 (2001)
35 L. Bedini, A. Tonazzini: Image Vision Comput. **10**, 108 (1992)
36 W.H. Press, S.A. Teukolsky, W.T. Vetterling, B.P. Flannery: *Numerical Recipes in C* (Cambridge University Press 1992) Chapt. 18, pp. 788–818
37 G. Golub, C.F. Van Loan: *Matrix Computations*, 3rd edn. (Johns-Hopkins University Press, Baltimore, MD 1996)
38 The MathworksTM, release 12, Natick, Massachusetts, MA
39 P.M. Morse, H. Feshbach: *Methods of Theoretical Physics*, Vol. I, Chapt. 8 (McGraw-Hill, New York 1953)
40 A. Tarantola: *Inverse Problem Theory: Methods for Data Fitting and Model Parameter Estimation* (Elsevier, Amsterdam 1987)
41 V.A. Morozov: *Methods for Solving Incorrectly Posed Problems* (Springer, Berlin 1984)
42 P.C. Hansen: Inverse Probl. **8**, 849 (1992)
43 S.W. Fu, J.F. Power: Appl. Spectrosc. **54**, 127 (2000)
44 T.E. Milner, D.M. Goodman, B.S. Tanenbaum, B. Anvari, L.O. Svaasand, J.S. Nelson: Phys. Med. Biol. **41**, 31 (1996)